Submitted to
33nd International Conference on High Energy Physics, ICHEP06, July. 26-Aug. 2, 2006, Moscow
Abstract:
Parallel Session: Soft QCD
www-h1.desy.de/h1/www/publications/conf/conf_list.html

Measurement and interpretation of the diffractive cross section at medium Q^2

H1 Collaboration

Abstract

Measurements of the diffractive cross section for the process $ep \to eXY$ are presented in the kinematic region $12 \leq Q^2 \leq 90$ GeV^2, $0.01 \leq \beta \leq 0.65$ and $x_{I\!P} < 0.1$, with $M_Y < 1.6$ GeV and $|t| < 1.0$ GeV^2, for an integrated luminosity of 68 pb^{-1}. These measurements are done using data taken with the H1 detector in the years 1999, 2000 and 2004, after selecting diffractive events showing a large rapidity interval between the hadronic systems X and Y. For the period 1999-2000 (corresponding to an integrated luminosity of 34 pb^{-1}), we present also a determination of the cross sections using a method, based on the difference of the dependence in M_X of the diffractive and standard inclusive contributions of the deep inelastic sample. Both approaches are compared in the kinematic range of the analysis, showing a nice agreement for the all Q^2 range. Then, together with previous data, the diffractive structure function measurements are analysed with a model based on the dipole formulation of diffractive scattering. It is found to give a very good description of the data over the all kinematic range.

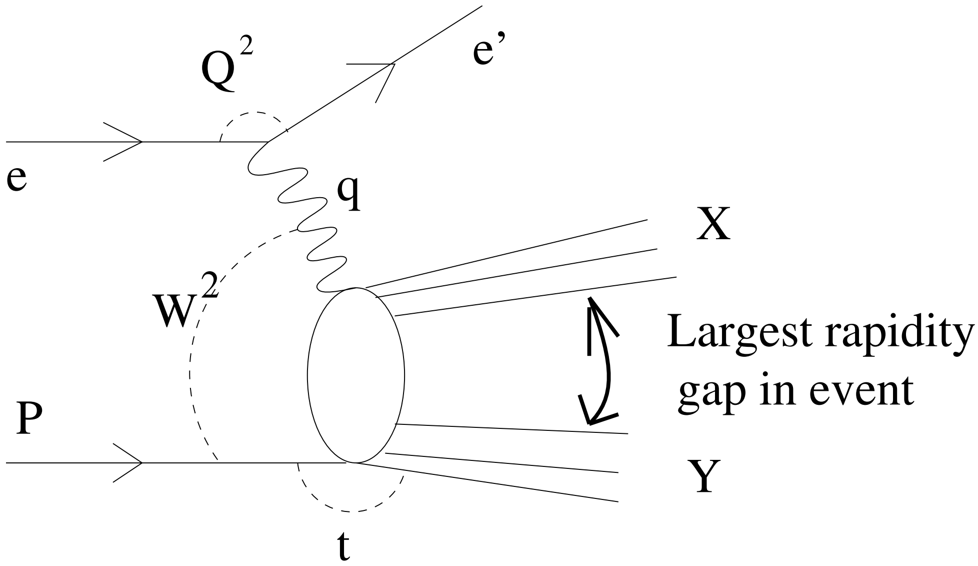

Figure 1: Illustration of the process $ep \to eXY$. The hadronic final state is composed of two distinct systems X and Y, which are separated by the largest interval in rapidity between final state hadrons.

1 Introduction

In this paper, we report measurements of the diffractive cross section based on deep-inelastic scattering (DIS) data taken during the years 1999, 2000 and 2004 by the H1 collaboration, with an integrated luminosity of 68 pb^{-1}, which is six times larger that in previous measurements in a comparable kinematic domain [1]. In the procsess $ep \to eXY$, the two distinct hadronic systems X and Y are separated by the largest interval in rapidity between final state hadrons. The system Y is closest to the direction of the outgoing proton beam (see Fig. 1).

The kinematics of the process can be described by the invariant masses M_X and M_Y of the systems X and Y, and the Lorentz scalars

$$x = \frac{-q^2}{2P \cdot q} \qquad y = \frac{P \cdot q}{P \cdot k} \qquad Q^2 = -q^2 \qquad t = (P - P_Y)^2 \, , \tag{1}$$

where P and k are the 4-momenta of the incident proton and electron respectively, P_Y is the 4-momentum of system Y and q is the 4-momentum of the exchanged virtual photon. The following variables are also defined:

$$\beta = \frac{-q^2}{2q \cdot (P - P_Y)} = \frac{Q^2}{Q^2 + M_X^2 - t} \qquad x_{I\!P} = \frac{q \cdot (P - P_Y)}{q \cdot P} = \frac{Q^2 + M_X^2 - t}{Q^2 + W^2 - M_P^2} = \frac{x}{\beta} \, , \tag{2}$$

where $W^2 = (q + P)^2$ is the center of mass energy squared of the virtual photon-proton system, M_P the proton mass and x is the Bjorken scaling variable.

2 Experimental Procedure

2.1 H1 Detector

A detailed description of the H1 detector can be found in [3]. Here only the detector components relevant for the present analysis are described. The SpaCal [4], a lead scintillating fibre calorimeter, covers the backward[1] region of the H1 detector ($153^\circ < \theta < 177.5^\circ$). Its energy resolution for electromagnetic showers is $\sigma(E)/E \simeq 7.1\%/\sqrt{E/\mathrm{GeV}} \oplus 1\%$. The liquid argon (LAr) calorimeter ($4^\circ \leq \theta \leq 154^\circ$) is situated inside a solenoidal magnet. The energy resolution for electromagnetic showers is $\sigma(E)/E \simeq 11\%/\sqrt{E/\mathrm{GeV}}$ as obtained from test beam measurements [5]. The backward drift chamber (BDC), placed in front of the SpaCal, measures track segments for charged particles entering the SpaCal from the interaction region. These are used to identify the scattered positron and to determine its position with a resolution of 0.5 mm in the radial and 2.5 mm in the azimuthal direction. The BDC was replaced by a backward proportional chamber (BPC) in 2004. The main component of the central tracking detector is the central jet chamber (CJC) which consists of two 2 m long coaxial cylindrical drift chambers, with wires parallel to the beam direction. The measurement of charged particle transverse momenta is performed in a magnetic field of 1.15 T, uniform over the full tracker volume. The forward components of the detector, used here to tag hadronic activity at large pseudo-rapidity ($5 \lesssim \eta \lesssim 7$), are the forward muon detector (FMD) and the proton remnant tagger (PRT). The FMD, designed to identify muons emitted in the forward direction, contains six planes of drift cells. It is used here to detect the particles produced when a proton dissociates and secondary interactions occur in the beampipe and adjacent material. Secondary particles, or the scattered proton, can also be detected by the PRT for the period 1999–2000, which is located at 24 m from the interaction point and consists of layers of scintillator surrounding the beam pipe. The luminosity measurement is based on the Bethe-Heitler process $ep \rightarrow ep\gamma$, where the photon is detected in a calorimeter located downstream of the interaction point.

2.2 Deep-inelastic selection

The data samples used for the intermediate Q^2 measurement correspond to an integrated luminosity of 34 pb^{-1} for the period 1999-2000 and again 34 pb^{-1} for the year 2004. Events were triggered by requiring a localised energy deposit (cluster) in the SpaCal calorimeter with an energy greater than 10 GeV, with a trigger efficiency close to 100 %. The cluster radius of the positron candidate was required to be less than 3.5 cm which is typical for an electromagnetic shower. A track segment was required in the backward tracker, matching the cluster in the SpaCal calorimeter to within 3 cm for 1999–2000 and 4 cm for 2004. In order to avoid losses of energy into the beampipe, events with more than 1 GeV of energy deposited in the veto layer of the SpaCal calorimeter were rejected and the radial distance between the beam axis and the point at which the extrapolated backward track intersects the surface of the SpaCal was required to be larger than 11 cm for 1999-2000 and 20 cm for 2004.

[1]H1 uses a right-handed coordinate system with z axis along the beam direction, the $+z$ or “forward” direction being that of the outgoing proton beam. The polar angle θ is defined with respect to the z axis and the pseudo-rapidity is given by $\eta = -\ln\tan\theta/2$.

Cosmic and beam induced backgrounds were reduced to negligible levels by requiring a vertex reconstructed within 30 cm of the nominal interaction point and that the timing of the signals from the tracking detector be within the interval expected for ep collisions. Radiative events and photoproduction events in which a hadron is misidentified as the scattered electron were suppressed by requiring $\Sigma(E - Pz) > 35$ GeV, where the sum extends over all final state hadrons and the scattered positron.

2.3 Rapidity gap selection

In a first approach, to select a subsample of events where a colourless exchange dominates, it is required that no signal is recorded above noise levels in a number of forward components of H1. The following conditions must be satisfied :

- no cluster with energy greater than 400 MeV in the forward part of the LAr calorimeter ($\eta > 3.2$).
- at most one hit pair in the first two layers of the FMD.
- for 1999–2000 period only, no signal in the PRT.

These selection criteria imply that the systems X and Y are well separated and that X is fully contained in the main part of the H1 detector. The system Y goes unobserved into the beam pipe, implying that $M_Y \leq 1.6$ GeV, and $|t| \leq 1$ GeV^2. In this analysis, we require also M_X to be above 4 GeV.

In a second step (section 3.2), the diffractive sample selection will be based on its difference in shape for the M_X spectrum with the standard inclusive sample. Then, no cut on the forward part of the liquid argon calorimeter will be applied, but the selection using FMD and PRT signals will be kept.

2.4 Kinematic reconstruction

The reconstruction method of the kinematic variables x, y and Q^2 is based on positron variables

$$Q^2_e = 4E'_e E_e \cos^2\frac{\theta_e}{2} \qquad\qquad y_e = 1 - \frac{E'_e}{E_e}\sin^2\frac{\theta_e}{2}\ , \tag{3}$$

where E_e is the positron beam energy and E'_e and θ_e are respectively the energy and polar angle of the scattered positron.

The mass of the X system M_X is used to compute $x_{I\!P}$ and β according to equation (2). Its reconstruction combines information from the calorimeters and vertex fitted tracks in the central tracker without double counting, which defined the reconstructed hadronic final state $(E, P_X, P_Y, P_Z)_h$ and the invariant mass M_X as :

$$M_X = f\sqrt{(E^2 - P_z^2 - P_T^2)_h \frac{y_e}{y_h}} \tag{4}$$

with $y_h = (E - P_Z)_h / 2E_e$. The factor y_e/y_h is included to improve the resolution at large y, where losses in the backward direction becomes large. The global factor f corrects for the residual looses of about 10 % (mainly located in the forward direction). The kinematic reconstruction method used here leads to the best resolution in the kinematic range of this analysis (at medium Q^2) and results are found in very good agreement with two other reconstruction methods that have been used in previous measurements [1, 2].

3 Cross section and structure function measurement

3.1 Large rapidity gap method

The large rapidity gap (LRG) sample defined previously (section 2.3) is used to measure the differential reduced cross section $\mathrm{d}^3\sigma_{red}^{D(3)}/\mathrm{d}Q^2\mathrm{d}\beta\mathrm{d}x$ for the process $ep \to eXY$, defined as :

$$\sigma_{red}^{D(3)}(Q^2, \beta, x) = \frac{\beta^2 Q^4}{4\pi\alpha_{em}^2} \frac{1}{(1 - y - \frac{y^2}{2})} \frac{\mathrm{d}^3\sigma_{ep\to eXY}}{\mathrm{d}Q^2\,\mathrm{d}\beta\,\mathrm{d}x}\ , \tag{5}$$

with $\sigma_r^{D(3)} = F_2^{D(3)} - \frac{y^2}{1+(1-y)^2} F_L^{D(3)}$, such that $\sigma_r^{D(3)} = F_2^{D(3)}$ is a very good approximation, except at large $y = W^2/s$ with s the total energy in the ep collision.

The bins in Q^2, β and x are chosen such that they are always larger than the resolution [2]. The results are corrected to the region $M_Y < 1.6$ GeV, and $|t| \leq 1$ GeV^2 and are presented as a function of $x_{I\!P} = x/\beta$ in bins of Q^2 and β on Fig. 2 and 3. The diffractive sample corresponds to a few % of the total inclusive sample, as illustrated on Fig. 4.

Acceptance losses due to the cuts are evaluated bin by bin directly from the data or by using a Monte Carlo simulation of the detectors. Corrections for migrations in the kinematic variables due to the finite resolution are determined using Monte Carlo programs with a full simulation of the H1 detector in its configuration during the period in which the data were taken. Diffractive DIS is modelled using the RAPGAP Monte Carlo model [6]. In RAPGAP is implemented the exchange of a partonic pomeron or meson with leading order QCD matrix elements describing the deep-inelastic scattering of the positron from the colourless exchange. The pomeron, meson flux and parton distributions are determined from previous data. Higher order QCD corrections are provided by the colour dipole model as implemented in ARIADNE [7]. At low M_X, where the presence of meson resonances ρ, ω, ϕ become important, the additional Monte Carlo model DIFFVM [8] is used. Migrations into the sample from the region $M_Y > 5$ GeV are studied with the additional use of the DJANGO Monte Carlo simulation [9] of inclusive deep-inelastic ep scattering.

Background from ep interactions arises from photoproduction events ($Q^2 \sim 0$) in which the positron signal is faked by a hadron detected in the SpaCal calorimeter. It is estimated using the PHOJET Monte Carlo model [10] and found to be negligeable in this analysis. Other backgrounds, such as that due to interactions of the beams with the remaining gas in the beam pipe or with beam line elements upstream of the H1 detector, are also found to be negligible.

The correction required for migrations around the limit of the measurement $M_Y < 1.6$ GeV is determined using a RAPGAP simulation containing processes both where the proton dissociates and where it remains intact. This correction is 9 ± 6 % in 1999–2000 and 18 ± 10 % in 2004.

Fluctuations in the level of noise in the forward detector components result in some events being wrongly rejected from the samples. The losses due to noise are determined using randomly triggered events and corrected on an event by event basis.

Radiative corrections are calculated bin by bin using the HERACLES program [11] interfaced to RAPGAP. They are smaller than 10 % for all measured data points. Bin centre corrections are performed based on a parameterizations of previous data with a dipole approach (see section 4).

3.2 M_X method and discussion

Another method to extract the diffractive contribution is proposed in [12]. Using the data taken during period 1999-2000, corresponding to an integrated luminosity of 34 pb^{-1}, we reproduce this kind of analysis and compare results with the cross sections derived from the LRG sample.

In a good approximation, the $\ln M_X^2$ spectrum in DIS can be described by the following form :

$$\frac{dN}{d \ln M_X^2} = D + c \cdot \exp(b \ \ln M_X^2), \ \ln M_X^2 < \ln W^2 - \eta_0, \tag{6}$$

where D is the diffractive contribution and the second term represents the non-diffractive contributions. The quantity $(\ln W^2 - \eta_0)$ specifies the maximum value of $\ln M_X^2$ up to which the exponential behaviour of the non-diffractive contribution holds. These different contributions are represented on Fig. 5. Note that the diffractive contribution is expected to be a slowly varying function of $\ln M_X^2$ when $M_X^2 > Q^2$, and to approach an approximately constant $\ln M_X^2$ distribution only for large M_X^2. Therefore, this diffractive part is not taken from the fit (D) but is obtained from the observed number of events after subtracting the non-diffractive contribution determined using the fitted values of b and c. In order to reduce the fluctuations of the method, we have fixed b to its mean value for the kinematic range of the measurement: $b_0 = 1.37 \pm 0.15$, where the uncertainty represents the statistical and systematical errors added in quadrature. Results are presented on Fig. 6 for the diffractive cross section differential in M_X (expressed in the $\gamma^* p$ reference frame) and compared with ZEUS published measurements [12]. We have corrected our cross section values to the region $M_Y < 2.3$ GeV, and $|t| \leq 1$ GeV^2, which is the domain used by the ZEUS collaboration in Ref. [12].

On Fig. 7, these measurements are converted in the laboratoty reference frame and expressed in the form of the reduced cross section. Then, they are compared to the results of the previous section, using the LRG sample. We notice the good agreement between both approaches in the kinematic range accessed by this analysis. This is also the case when we convert the ZEUS measurements in the same form, as illustrated on Fig. 7 and 8. Scaling violations for both samples (determined for the 1999–2000 period) are presented on Fig. 9.

4 Good and Walker inspired model

In these kind of description of the diffractive scattering [16], there are different ways to describe the interaction of a diffractive Fock state of the virtual photon with the proton. In this paper, we consider the two gluon exchange model for this interaction. In Ref. [17], a parameterisation of the diffractive structure function in terms of three main contributions is proposed. More explicitely, we consider its modified form proposed in Ref. [12]. In this model, the photon fluctuates into partonic states which scatter diffractively, the pomeron being modelled by the exchange of two gluons from the proton. The simplest description of diffractive DIS starts from the process of $q\bar{q}$ production, which is described here in terms of light-cone wave-functions in the proton rest frame. The light cone wave function of the photon gives the partonic content of the photon. At the beginning of the scattering process, the photon splits into a $q\bar{q}$ pair, and at sufficient M_X^2, the $q\bar{q}$ pair can radiate an additional gluon before it reaches the proton at rest. At small diffractive masses, it is expected that the longitudinal cross section for $q\bar{q}$ pair production is not small compared to the tranverse cross section.

The first contribution $F_2^{D(3)}(q\bar{q}_T)$ corresponds to the diffractive scattering of the transverse $q\bar{q}$ component of the photon. The second, $F_2^{D(3)}(q\bar{q}g_T)$, corresponds to the transverse $q\bar{q}g$ component, and the third, $F_2^{D(3)}(q\bar{q}_L)$, which gives a higher twist contribution, corresponds to the longitudinal $q\bar{q}$ component. The longitudinal part of the $q\bar{q}g$ term (which is also a higher twist contribution) is expected to be small compared to the transverse $q\bar{q}g$ term and is neglected. Thus, the three main contributions to $F_2^{D(3)}$ can be written :

$$F_2^{D(3)}(q\bar{q}_T) = A\left(\frac{x_0}{x_{I\!P}}\right)^{n_2}\beta(1-\beta) \tag{7}$$

$$F_2^{D(3)}(q\bar{q}g_T) = B\left(\frac{x_0}{x_{I\!P}}\right)^{n_2}\alpha_S\left(\ln[\frac{Q^2}{Q_0^2}+1]\right)(1-\beta)^{\gamma} \tag{8}$$

$$F_2^{D(3)}(q\bar{q}_L) = C\left(\frac{x_0}{x_{I\!P}}\right)^{n_4}\left(\frac{Q_0^2}{Q^2+Q_0^2}\right)\left(\ln[\frac{Q^2}{4Q_0^2\beta}+7/4]\right)^2\beta^3(1-2\beta)^2 \tag{9}$$

where

$$n_{2(4)} = n_{2(4)}^0 + n_{2(4)}^1 \ln\left[\frac{Q^2}{Q_0^2}+1\right]. \tag{10}$$

The free parameters in the fit are the three normalisation factors A, B and C, the n_2^0, n_4^0, n_2^1, n_4^1 factors which describe the $x_{I\!P}$ dependence of the cross section and are not predicted by QCD, and the γ parameter which describes the β dependence of the $q\bar{q}g$ term. An additional free parameter, x_0, was introduced to minimize any effect from n_2 and n_4 on the overall Q^2 shape. Q_0^2 is taken to be 1 GeV^2 and α_S is taken at the fixed value of 0.25. Also, a sub-leading trajectory [13] is added to the model, with an overall normalisation $n_{I\!R}$ as further free parameter and the value of $\alpha_{I\!R} = 0.5$.

A fit is performed to the structure functions derived in this paper with the data taken during the years 1999,2000 and 2004 data. Previous measurements [1] are also included in the fit, which gives a nice description of all data sets. The resulting value of γ is large (~ 10), leading to a strong β dependence of the $q\bar{q}g$ term, which is dominant only in the low β region. In this kinematic domain, contributions in which more than two partons emerge from the diffractive hard scattering have also been found to be important in measurements of hadronic final state observables in diffractive DIS [14, 15]. The longitudinal $q\bar{q}$ term becomes large for $\beta > 0.5$, indicating a strong higher twist contribution in this kinematic region. At intermediate β, the transverse $q\bar{q}$ term, varying as $\beta(1-\beta)$ is dominant. All these contributions are illustrated on Fig. 10 with data from the analysis reported in this paper for a few bins in Q^2. Points from the previous H1 measurements [1] converted to the $x_{I\!P}$ value quoted for this figure are also presented. In particular, we notice the good comaprison between the prediction of the fit and the experimental results.

This shows that the scaling violations of $F_2^{D(3)}$ observed experimentally and discussed in the previous section can be described by the Q^2 dependence of the $q\bar{q}$ term at medium β because the exponent of $x_{I\!P}$ depends on Q^2. They can be indirectly generated by a Q^2 dependence of the $x_{I\!P}$s distribution.

5 Conclusion

Diffractive cross section measurements have been realised in the kinematic region $12 \leq Q^2 \leq 90$ GeV^2, $0.01 \leq \beta \leq 0.65$ and $x_{I\!P} < 0.1$, with $M_Y < 1.6$ GeV and $|t| < 1.0$ GeV^2, for an integrated luminosity of 68 pb^{-1}. Two methods have been applied to determine diffractive samples, based on a rapidity gap selection and on the behaviour in M_X of the diffractive cross section. Both approaches are in good agreement and are also in good agreement with previous H1 and ZEUS measurements in the kinematic domain considered in this analysis. Then, the diffractive structure function measurements have been compared with a model based on the dipole formulation of diffractive scattering, which gives a very good description of the data.

References

[1] A. Aktas*et al.*, [H1 Collaboration], [hep-ex/0606004].

[2] T. Nicholls, PhD Thesis, Univ. of Birmingham, April 1997;
T. Nicholls, C. Royon, L. Schoeffel, A. Van Haecke, H1 note H1-IN-567 (1999).

[3] I. Abt *et al.* [H1 Collaboration], Nucl. Instrum. Meth. A **386** (1997) 310 and 348.

[4] R.D. Appuhn *et al.* [H1 SPACAL Group], Nucl. Instrum. Meth. A **386** (1997) 397.

[5] B. Andrieu *et al.* [H1 Calorimeter Group], Nucl. Instrum. Meth. A **350** (1994) 57.

[6] H. Jung, Comp. Phys. Commun. 86 (1995) 147.

[7] L. Lönnblad, Comp. Phys. Commun. 71 (1992) 15.

[8] B. List, Diploma Thesis, Tech. Univ. Berlin, unpublished.

[9] G. Schuler, H. Spiesberger, Proceedings of the Workshop on "Physics at HERA", vol 3, eds. W. Buchmüller, G. Ingelman, DESY (1992) 317.

[10] R. Engel, Z. Phys. **C66** (1995) 203;
R. Engel, J. Ranft, Phys. Rev. **D54** (1996) 4244.

[11] A. Kwiatkowski, H. Spiesberger, H.-J. Möhring, Comp. Phys. Commun. 69 (1992) 155.

[12] S. Chekanov *et al.* [ZEUS Collaboration], Nucl. Phys. **B713** (2005) 3.

[13] M. Glück, E. Reya, A. Vogt, Z. Phys. **C53** (1992) 651.

[14] C. Adloff *et al.* [H1 Collaboration], Eur. Phys. J. **C1** (1998) 495.

[15] C. Adloff *et al.* [H1 Collaboration], Phys. Lett. **B428** (1998) 206, hep-ex/9803032;
C. Adloff *et al.* [H1 Collaboration], Eur. Phys. J. **C5** (1998) 439, hep-ex/9804012.

[16] M.L. Good and W.D. Walker, Phys. Rev. **D120** (1960), 1857.

[17] J. Bartels, J. Ellis, H. Kowalski, M. Wuesthoff, Eur. Phys. J. **C7** (1999) 443;
J. Bartels, C. Royon, DESY 98-152 [hep-ph/9809344].

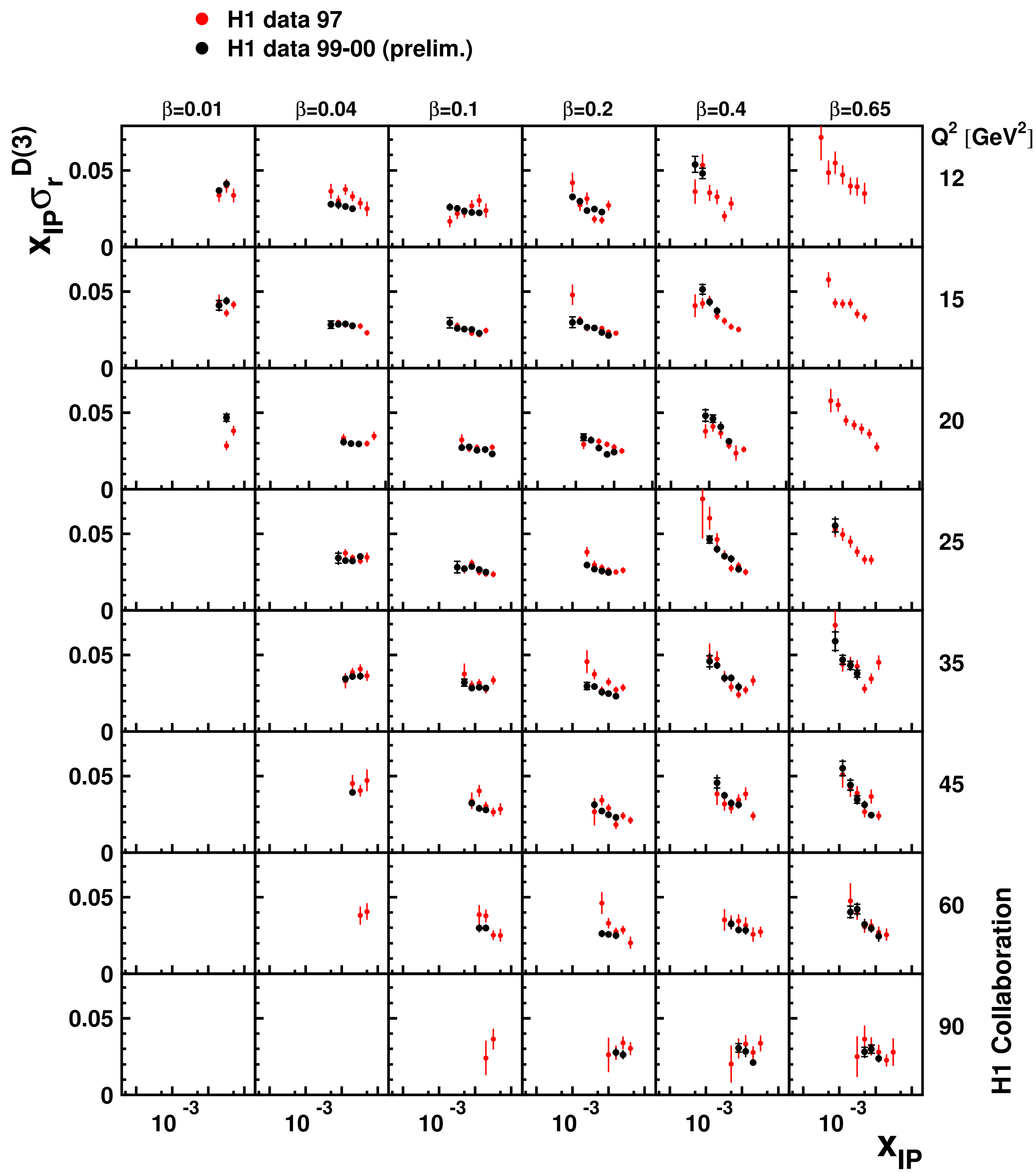

Figure 2: Reduced cross sections $x_{I\!P}\sigma_{red}^{D(3)}$ of this analysis for the period 1999–2000, compared to published H1 measurements with the year 1997.

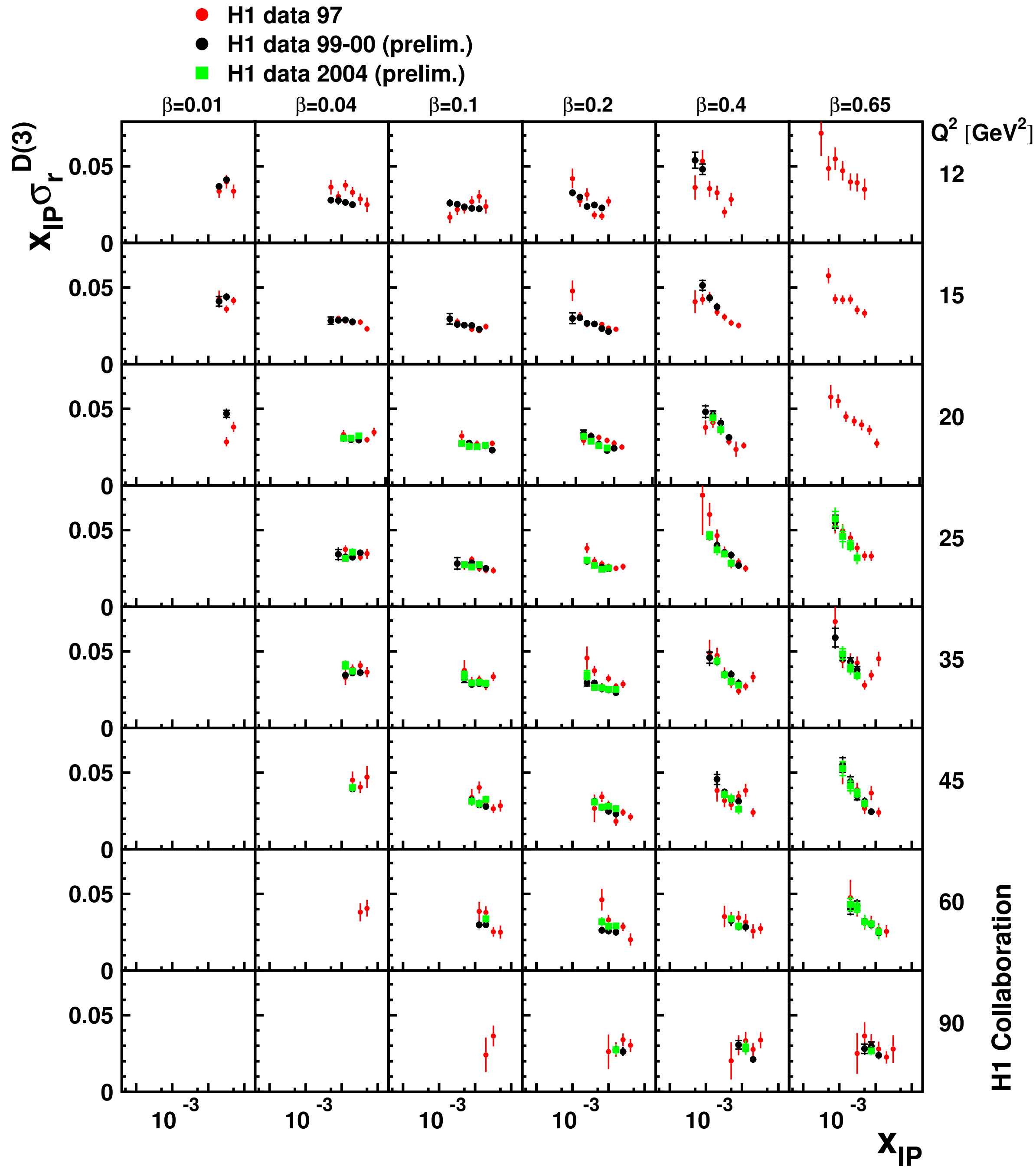

Figure 3: Reduced cross sections $x_{I\!P}\sigma_{red}^{D(3)}$ of this analysis for the years 1999–2000 and 2004, compared to published H1 measurements with the year 1997.

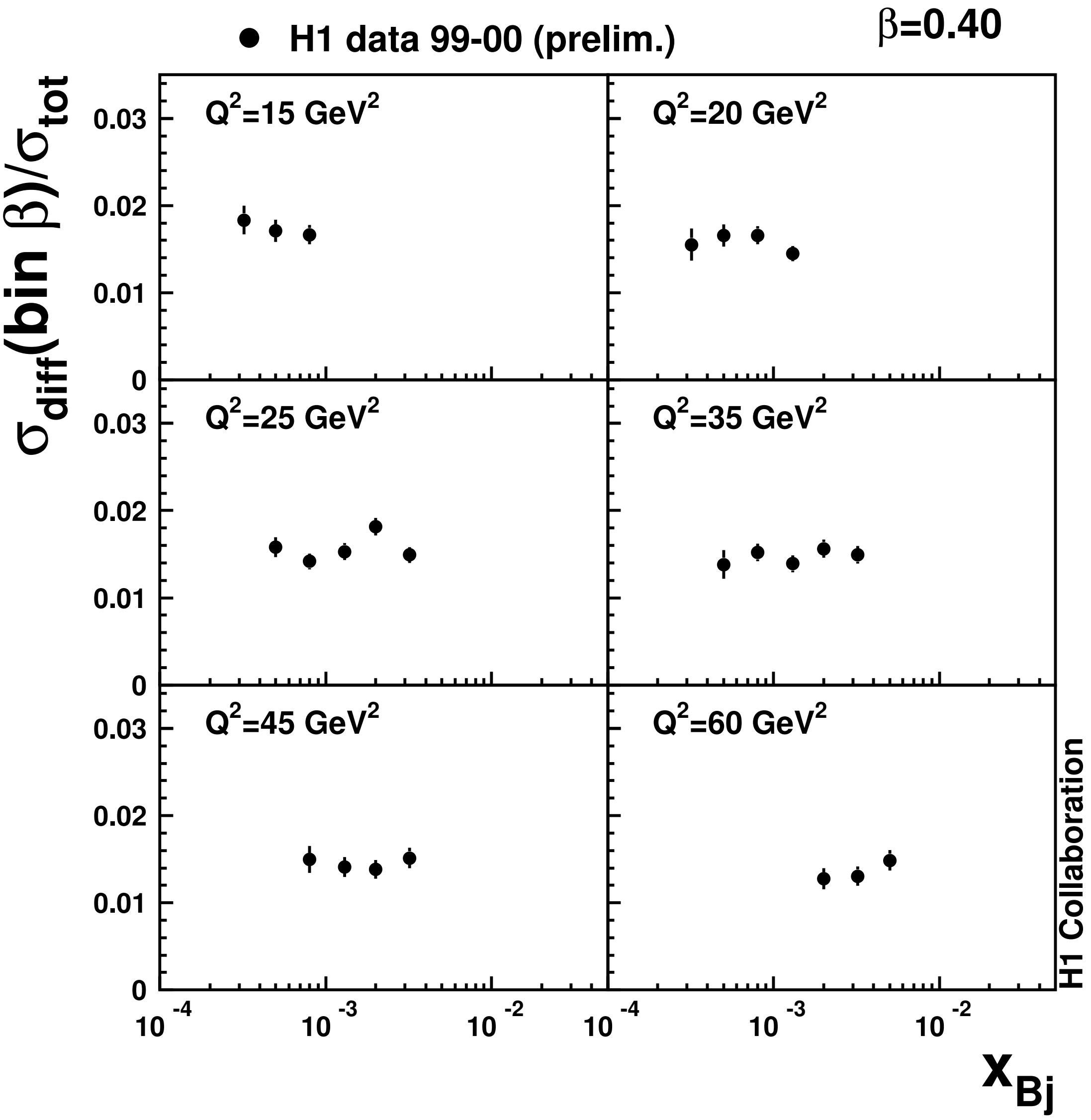

Figure 4: Ratio of the diffractive cross section with the total cross section.

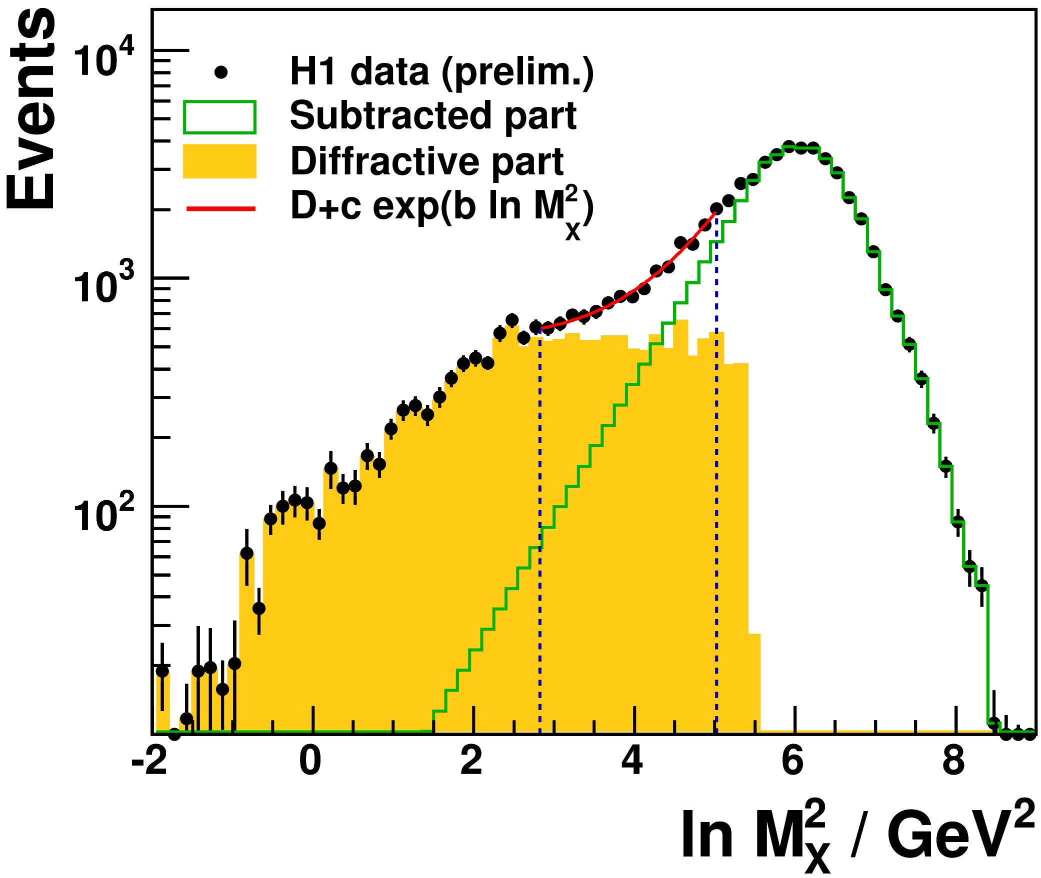

Figure 5: $\ln M_X^2$ spectra with the different contributions (see text).

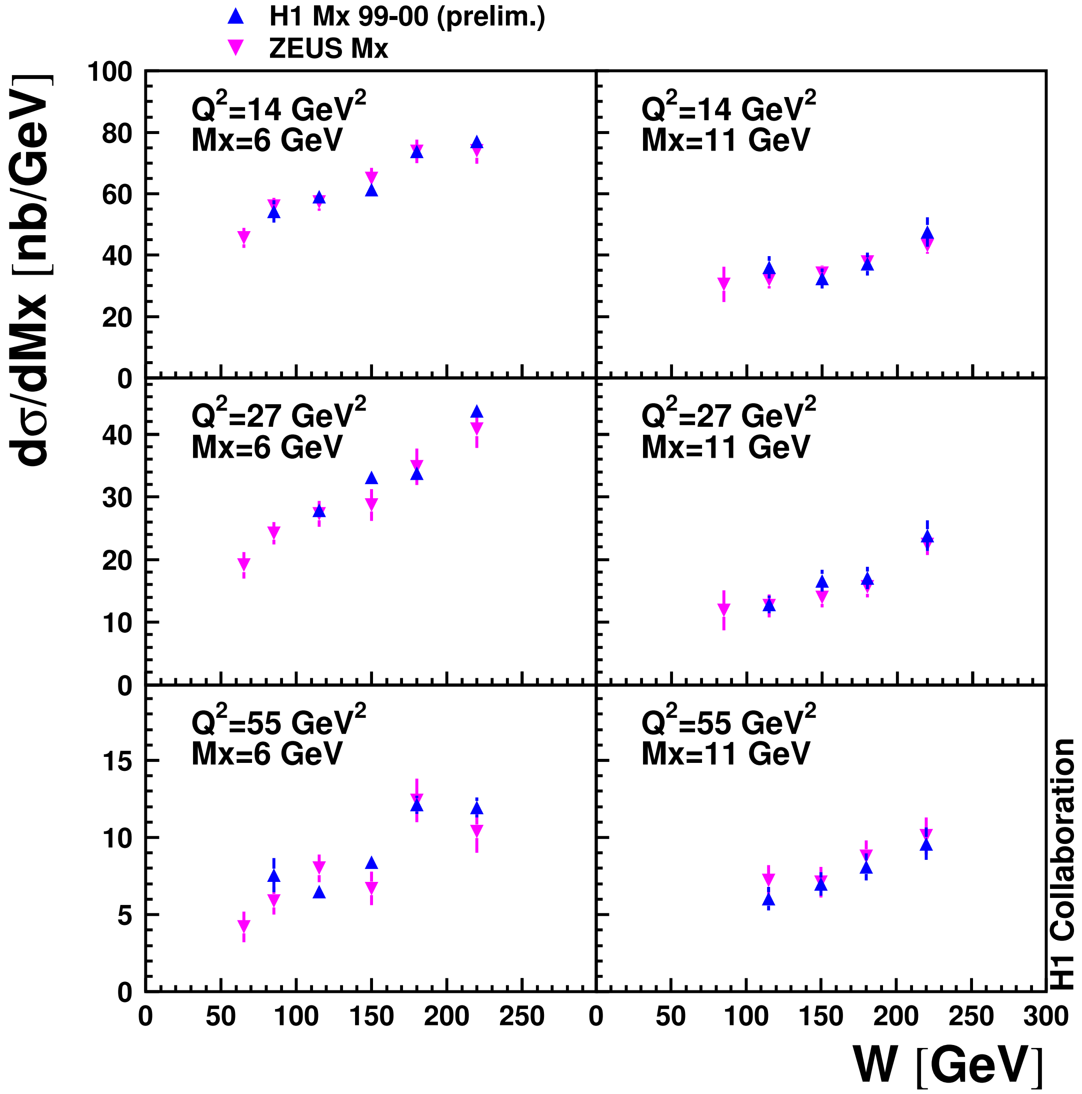

Figure 6: Cross section measurements (converted in the $\gamma^{*}p$ reference frame), differential in M_X, as a function of W for 3x3 bins of Q^2-M_X.

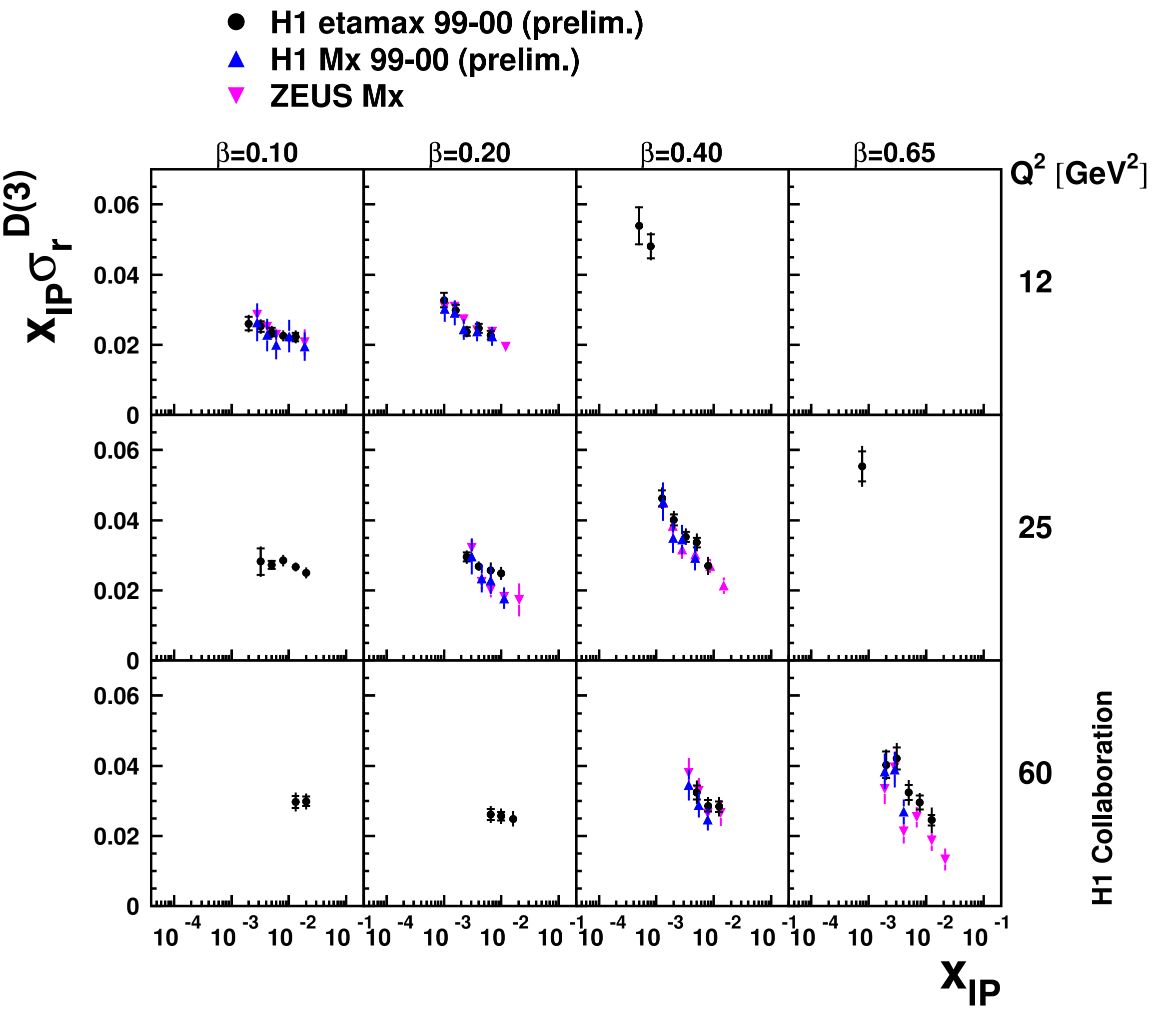

Figure 7: Comparisons of the diffractive reduced cross sections using the LRG and M_X samples for 1999–2000 data and ZEUS (see text).

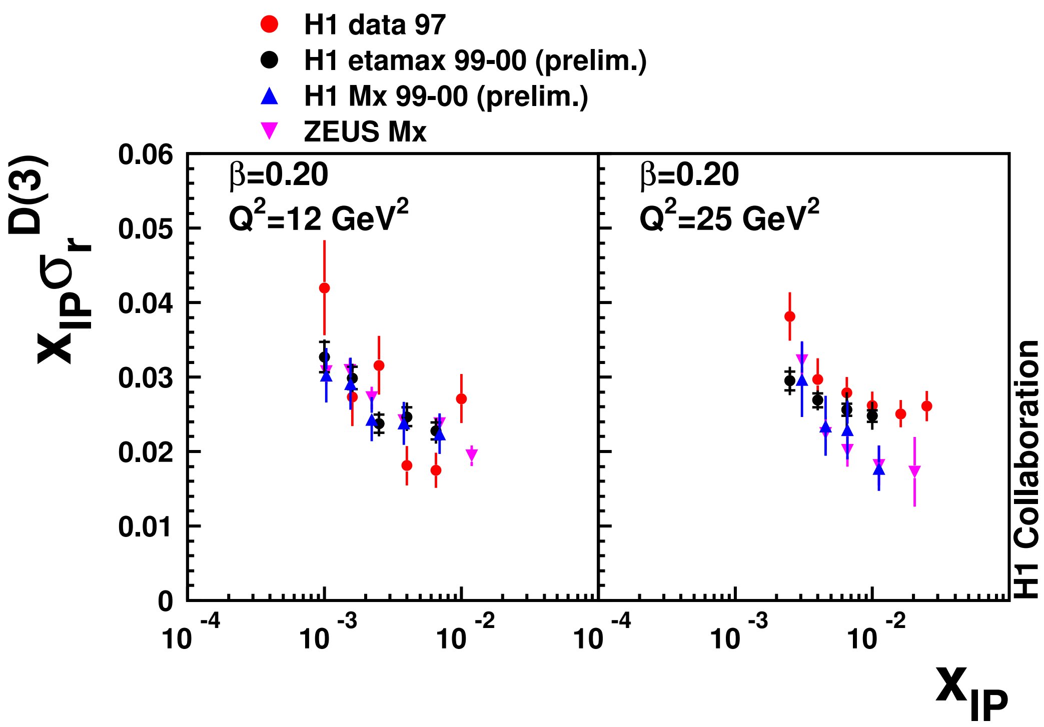

Figure 8: Comparisons of the diffractive reduced cross sections, zoomed in two bins, using the LRG and M_X samples for 1999–2000 data, ZEUS, and previous H1 measurements (see text).

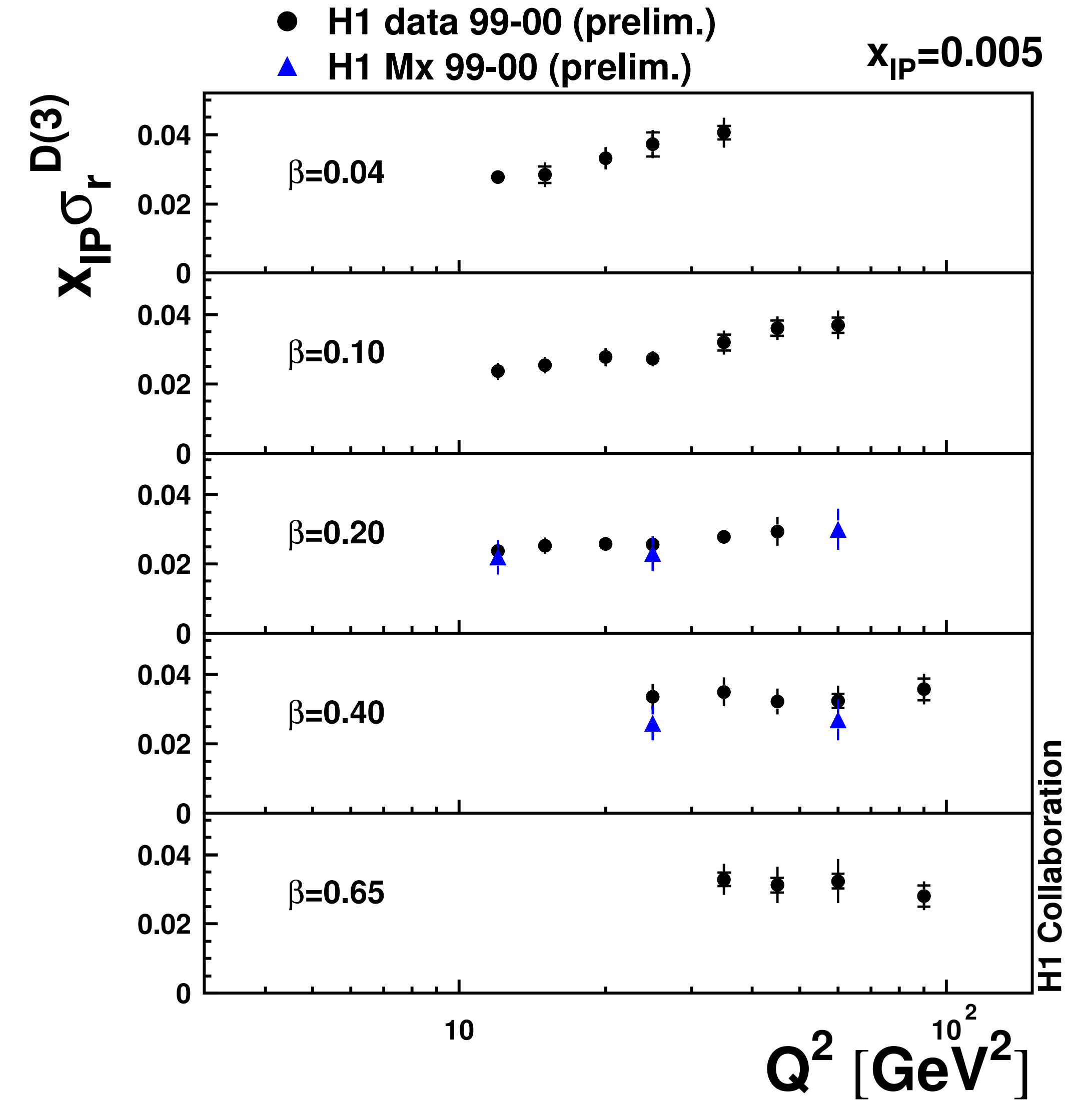

Figure 9: Scaling violations of the diffractive cross section measurements for both methods (see text).

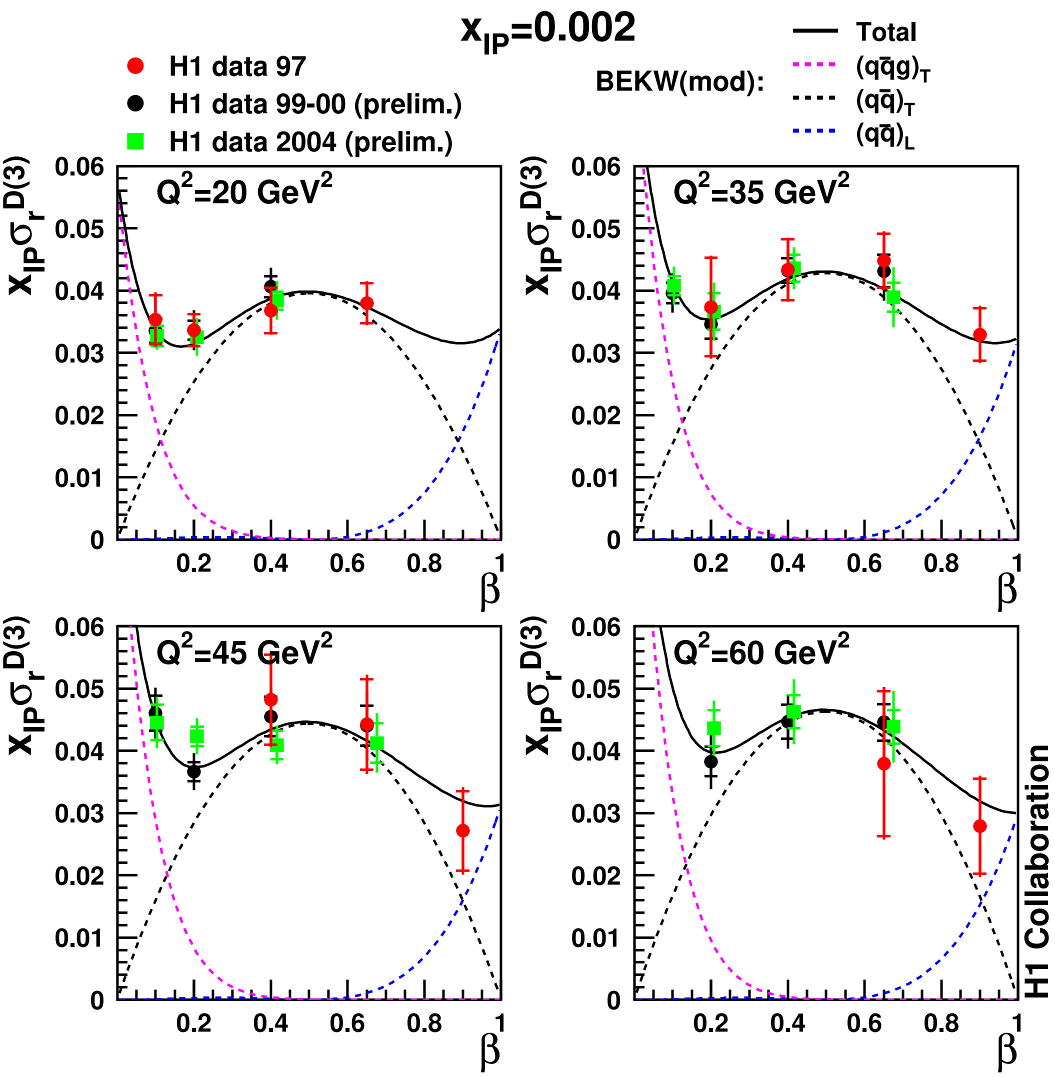

Figure 10: Comparisons of the diffractive cross section values of this analysis (1999–2000 and 2004) with the prediction of the two-gluon exchange model, fitted on these data and previous H1 measurements (also plotted here). Results are presented as a function of β, for different Q^2 values, for a fixed $x_{I\!P} = 0.002$ value.